


 Cite this: *RSC Adv.*, 2020, 10, 12129

# Incorporating Ni-MOF structure with polypyrrole: enhanced capacitive behavior as electrode material for supercapacitor†

 Baoling Wang,<sup>a</sup> Wei Li,<sup>a</sup> Zhelin Liu,<sup>a</sup> \*<sup>a</sup> Yujie Duan,<sup>a</sup> Bo Zhao,<sup>a</sup> <sup>ab</sup> Yin Wang<sup>b</sup> and Jinghai Liu <sup>b</sup>

Herein, Ni-MOF sheet incorporated with polypyrrole is fabricated *via* a simple wet-chemical approach, and the obtained PPy-MOF composite is investigated as an electrode material for supercapacitors. The composite is systematically investigated by a series of characterization studies including X-ray diffraction, scanning electron microscopy, and X-ray photoelectron spectroscopy. Besides that, the electrochemical capacitive behaviors of the products are examined by electrochemical measurements. Electrochemical results show varying the ingredient ratio can lead to different electrocapacitive behavior, and PPy-MOF-0.2 is proved to possess the best performance in the investigated recipes. Furthermore, an asymmetric supercapacitor employing PPy-MOF and activated carbon as positive and negative electrodes is also assembled, which exhibits high energy density.

Received 12th December 2019

Accepted 6th March 2020

DOI: 10.1039/c9ra10467d

[rsc.li/rsc-advances](http://rsc.li/rsc-advances)

## Introduction

With rapid population growth and socio-economic development, environmental problems caused by the use of non-renewable resources have become more and more serious. Research and development of a new highly efficient and environmentally friendly renewable resource have become important choices for the sustainable development of society,<sup>1,2</sup> which in turn causes the rapid development of energy storage and energy conversion systems, such as supercapacitors,<sup>3</sup> fuel cells,<sup>4</sup> and lithium-ion batteries.<sup>5,6</sup> Conventional batteries possess high energy density and long energy life, but the power density is normally poor.<sup>7</sup> Compared with conventional batteries, supercapacitors, as a new kind of electrochemical energy storage device, have attracted widespread attention due to their high power density, fast charge/discharge capability and long cycle life.<sup>8,9</sup>

The metal-organic framework (MOF) is an organic-inorganic hybrid material with intramolecular pores formed by the self-assembly of organic ligands and metal ions or clusters by coordination bonds,<sup>10</sup> which has attracted great attention in terms of gas storage,<sup>11</sup> catalysis,<sup>12,13</sup> magnetism<sup>14</sup> and solar cell<sup>15</sup>

due to high porosity, large specific surface area, and diversity of structures and functions. By facilitating the charge storage and diffusion of the electrolyte, MOF can be applied as electrode material for supercapacitors,<sup>16</sup> which can increase pseudocapacitive redox centers owing to the electrochemical active sites.<sup>17</sup> However, the practical application of MOF as electrode material has been limited owing to its poor conductivity. One effective way to improve the conductivity of MOF is to bind it with other materials of high conductivity. For example, Zhou *et al.*<sup>18</sup> fabricated a series of novel Ni-MOFs@GO composites to serve as electrode materials, which showed excellent electrochemical energy storage performance.

Polypyrrole (PPy) is an ideal electrode material candidate in the field of supercapacitors due to its unique characteristics such as high conductivity, good thermal stability, fast charge and discharge mechanism, low cost and high energy density.<sup>19-21</sup> Up to now, PPy has been combined with many transition metal compounds as electrode materials which have greatly improved the electrochemical performance.<sup>22,23</sup> Thus, combining PPy of high conductivity with MOFs is expected to significantly facilitate the electron transfer, and this strategy has been developed in the fabrication of composite combining MOF with PPy as electrode materials for supercapacitors.<sup>24-28</sup> For example, Liu *et al.*<sup>24</sup> integrated ZIF-67 and PPy through electrochemical deposition technology, and the resulting composite was employed as electrode material which exhibited excellent electrocapacitive performance. To the best of our knowledge, flowerlike Ni-MOF/PPy composite as electrode material for supercapacitor has never been reported before.

Herein, Ni-MOF is incorporated with PPy to fabricate a new flowerlike electrode material PPy-MOF by a simple wet-chemical

<sup>a</sup>School of Chemistry & Environmental Engineering, Changchun University of Science and Technology, Changchun, Jilin 130022, P. R. China. E-mail: zl.liu@live.cn; Fax: +86-431-85583459; Tel: +86-431-85583459

<sup>b</sup>Inner Mongolia Key Laboratory of Carbon Nanomaterials, College of Chemistry and Chemical Engineering, Nano Innovation Institute, Inner Mongolia University for Nationalities, Tongliao, Inner Mongolia 028000, China

† Electronic supplementary information (ESI) available. See DOI: 10.1039/c9ra10467d



route. The morphology, chemical composition and electrochemical capacitive behavior of the as-prepared PPy-MOF are investigated. The effect of component ratio on the electrochemical property is examined. The optimum PPy-MOF is also assembled into an asymmetric supercapacitor, of which the electrocapacitive behavior is systematically studied.

## Experimental

### Materials

All chemicals including  $\text{Ni}(\text{NO}_3)_2 \cdot 6\text{H}_2\text{O}$ , terephthalic acid (TPA), *N,N*-dimethylformamide (DMF), pyrrole (Py),  $\text{FeCl}_3 \cdot 6\text{H}_2\text{O}$  and NaOH are of analytical grade and purchased from Sino-pharm Group (Shanghai, China). High purity water ( $18.2 \text{ M}\Omega \text{ cm}$ ) is used throughout the whole experiment.

### Synthesis of flower-like Ni-MOF

The flower-like Ni-MOF is synthesized according to the literature previously reported with slight modification.<sup>29</sup> In a typical synthesis, TPA (0.664 g) and  $\text{Ni}(\text{NO}_3)_2 \cdot 6\text{H}_2\text{O}$  (0.384 g) are dissolved in DMF (80 mL) with stirring at room temperature, and 4 mL of NaOH aqueous solution (0.4 M) is added into the above solution slowly. The mixture is transferred into a Teflon-lined stainless steel autoclave, which is heated at  $100 \text{ }^\circ\text{C}$  for 8 h, and then cooled to room temperature naturally. The resulting precipitate is centrifuged and washed several times with DMF and ethanol, respectively. The obtained precipitate is redispersed in ethanol and the dispersion is ultrasonicated for 1 h in iced water bath, and dried under vacuum at  $60 \text{ }^\circ\text{C}$  for 12 h.

### Synthesis of PPy

The preparation of polypyrrole (PPy) is carried out according to a previous method with slight modification.<sup>30</sup> In a typical experiment, 0.25 mL Py (1 M) aqueous solution is added slowly into a 2.5 mL  $\text{FeCl}_3 \cdot 6\text{H}_2\text{O}$  (0.1 M) aqueous solution under magnetic stirring and  $\text{Ar}_2$  flow at  $8 \text{ }^\circ\text{C}$ , and 3 mL water is added to the above solution, obtaining the mixture. After 2 h of stirring, the product is centrifuged, washed with water, ethanol and acetone several times respectively and dried at  $60 \text{ }^\circ\text{C}$  for 4 h.

### Synthesis of PPy-MOF

The synthesis of PPy-MOF is similar to the preparation of PPy. The difference is introducing certain amount of Ni-MOF dispersion into the mixture obtained in the above section during the stirring process. Thus, a series of PPy-MOF composites with different mass of Ni-MOF are synthesized for comparison, and are abbreviated as PPy-MOF-*x* ("*x*" is the mass of Ni-MOF, that is, 0.05, 0.1, 0.15, 0.2, or 0.3 g).

### Characterizations

The phase purity and crystallinity of the materials are characterized by X-ray diffraction (XRD) on D/max 2550. Fourier transform infrared (FTIR) analyses of the samples are carried out on FTIR-8400s spectrometer. The scanning electron microscopy (SEM) and energy dispersive X-ray spectroscopy

(EDS) images of the samples are obtained by employing an XL 30ESEM-FEG. X-ray photoelectron spectroscopy (XPS) is carried out on ESCALAB 250.

### Electrochemical measurements in a three-electrode system

The prepared products are used as active electrode material, which is mixed with acetylene black (15 wt%), polyvinylidene fluoride (PVDF, 5 wt%), and 1-methyl-2-pyrrolidinone (NMP) to form a homogenous slurry. The slurry is then coated onto a nickel foam ( $1 \text{ cm} \times 1 \text{ cm}$ ), which is dried at  $110 \text{ }^\circ\text{C}$  for 12 h under a vacuum circumstance and then pressed under a pressure of 10 MPa. The average mass loading of the active material is about  $5 \text{ mg cm}^{-2}$ . The modified nickel foam is used as working electrode, of which the electrochemical properties are investigated on a CHI660E electrochemical workstation (Chenhua, Shanghai, China) with a typical three-electrode system in 3 M KOH solution. The platinum wire and Hg-HgO electrode are served as counter electrode and reference electrode, respectively. Cyclic voltammetry (CV), galvanostatic charge-discharge (GCD) and electrochemical impedance spectroscopy (EIS) tests are performed. The specific capacitance  $C_s$  ( $\text{F g}^{-1}$ ) of the PPy-MOF composite is calculated from the galvanostatic discharge process according to the following equation.<sup>31,32</sup>

$$C_s = I\Delta t / (m\Delta V) \quad (1)$$

where  $I$  (A) represents the current,  $\Delta t$  (s) is the discharge time,  $\Delta V$  (V) corresponds to the potential window, and  $m$  (g) is the mass of the active material.

### Fabrication of asymmetric supercapacitor

A simple asymmetric supercapacitor (ASC) is assembled using PPy-MOF-0.2 and activated carbon (AC) modified nickel foam as positive and negative electrodes, respectively. The modified nickel foam is fabricated in the similar way as described in the above section. The mass loading of the active material on the positive electrode is  $5 \text{ mg cm}^{-2}$ . In the ASC, 3 M KOH aqueous solution is used as the electrolyte. The energy density  $E$  ( $\text{W h kg}^{-1}$ ) and power density  $P$  ( $\text{W kg}^{-1}$ ) are calculated as follows.<sup>33</sup>

$$E = C_s \Delta V^2 / 7.2 \quad (2)$$

$$P = 3600E / \Delta t \quad (3)$$

## Results and discussion

The PPy-MOF composites are successfully synthesized by introducing Ni-MOF in the process of PPy polymerization. PPy-MOF-0.2 is selected as the example for morphology and composition characterization of PPy-MOF. XRD and FTIR are firstly used to explore the structure and composition of PPy-MOF. The XRD patterns of Ni-MOF and PPy-MOF are shown in Fig. 1A. The diffraction peaks of Ni-MOF are consistent with the literature previously reported,<sup>29</sup> indicating that Ni-MOF is prepared successfully. The XRD pattern of PPy-MOF is similar to



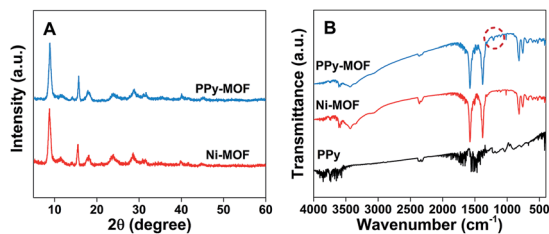


Fig. 1 (A) XRD patterns of PPy-MOF-0.2 and Ni-MOF, (B) FTIR spectra of PPy-MOF-0.2, Ni-MOF, and PPy.

that of Ni-MOF, suggesting that the structure of Ni-MOF is not destroyed during the polymerization of pyrrole. Besides, for PPy-MOF composite, no obvious diffraction peaks of PPy are observed owing to its noncrystalline structure. The FTIR spectra of PPy, Ni-MOF, and PPy-MOF are shown in Fig. 1B. For Ni-MOF, the bands at 3596 and 1508  $\text{cm}^{-1}$  are respectively attributed to the stretching vibrations of  $-\text{OH}$  and *para*-aromatic  $-\text{CH}$  groups.<sup>29</sup> The characteristic peaks at 3435, 3350 and 3066  $\text{cm}^{-1}$  indicate that  $\text{H}_2\text{O}$  molecules are present within the Ni-based material.<sup>2,29</sup> In addition, the strong bands at 1390 and 1582  $\text{cm}^{-1}$  are attributed to the stretching vibration of  $-\text{COO}^-$  group.<sup>29</sup> These results confirm that the synthesized Ni-MOF is a kind of nickel hydroxyl-terephthalate-based compound. For PPy, a breathing vibration is observed at 1211  $\text{cm}^{-1}$  and a band at 1467  $\text{cm}^{-1}$  is associated with the formation of C–N stretching vibration.<sup>34</sup> It can be seen that the FTIR spectrum of PPy-MOF is similar to Ni-MOF. Besides, the diffraction peak at 1211  $\text{cm}^{-1}$  characteristic of PPy can also be observed, showing the successful combination of Ni-MOF and PPy. EDS analysis is conducted to determine the elemental composition of the prepared PPy-MOF-0.2. As shown in Fig. S1,† peaks appeared in the EDS image confirm the existence of element Ni, C, O and N in the sample.

The surface morphology of the prepared Ni-MOF is analyzed by SEM. As shown in Fig. 2A, Ni-MOF displays a uniform flower-

like structure with a diameter of 10 microns. The high-magnified SEM image (Fig. 2B) reveals the thin sheet nanostructure on the prepared Ni-MOF. Fig. 2C is the SEM image of PPy, in which PPy exhibits an irregular globular structure with an average size of 0.5  $\mu\text{m}$ . The prepared Ni-MOF is further combined with PPy, and the morphology of the resultant composite is displayed in Fig. 2D. It can be seen that after the introduction of PPy, the surface of thin sheets on Ni-MOF is covered by PPy. Besides, the general morphology of Ni-MOF does not change obviously, indicating introducing PPy does not destroy the structure of Ni-MOF.

XPS test is conducted to explore the chemical bonding state of PPy-MOF, and the results are shown in Fig. 3. The XPS survey spectrum (Fig. S2†) demonstrates the presence of Ni, C, N, and O elements in PPy-MOF. In the high-resolution Ni 2p XPS spectrum (Fig. 3A), the fitting peaks at 857.1 eV and 874.7 eV correspond to Ni 2p<sub>3/2</sub> and Ni 2p<sub>1/2</sub>, respectively, while the spin-energy separation of Ni 2p<sub>3/2</sub> and Ni 2p<sub>1/2</sub> is 17.6 eV, which are characteristic of Ni<sup>2+</sup> and in accordance with previous reported literature.<sup>35,36</sup> Two broad peaks at 861.4 eV and 880.1 eV of Ni 2p<sub>3/2</sub> and Ni 2p<sub>1/2</sub> can be attributed to two satellites bands (“Sat.”), implying that Ni element exists in the form of divalent state, which is also in good agreement with previous report.<sup>37</sup> Fig. 3B is the N 1s XPS spectrum of PPy-MOF composite. It can be seen that three peaks appeared at 401.3 eV ( $-\text{N}^+$ ), 399.8 eV ( $-\text{NH}-$ ) and 398.2 eV ( $=\text{N}-$ ), demonstrating the successful fabrication of PPy.<sup>24</sup> Moreover, XPS spectrum of C 1s region (Fig. 3C) can be divided into three peaks located at 284.7, 285.6, and 288.2 eV, which can be assigned to C–C, C=O, and O–C=O, respectively.<sup>38,39</sup> In addition, the XPS spectrum of O 1s (Fig. 3D) is also obtained, which can be fitted into two peaks corresponding to the oxygen atoms in O=C–O (531.7 eV) groups of the terephthalic acid linker and  $-\text{OH}$  (532.8 eV).<sup>38</sup> The above-mentioned analyses indicate that the PPy-MOF composite are fabricated successfully.

Since both PPy and Ni-MOF are considered to possess the electrocapacitive capability, the resulting composite PPy-MOF is

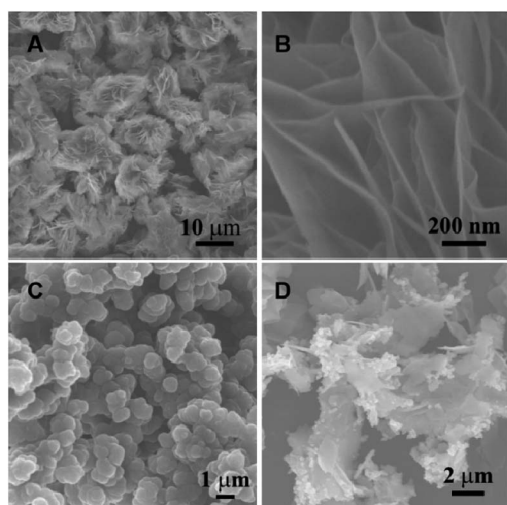


Fig. 2 SEM images of (A and B) Ni-MOF, (C) PPy, and (D) PPy-MOF.

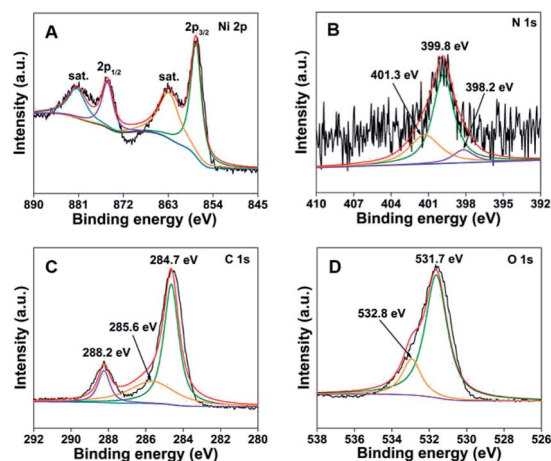


Fig. 3 XPS spectra of (A) Ni 2p, (B) N 1s, (C) C 1s, and (D) O 1s regions of PPy-MOF composite.



expected to exhibit good electrochemical behavior as electrode material for supercapacitors. Thus, the capacitive behavior of PPy-MOF with different composition ratios are firstly investigated in three-electrode system. Different PPy-MOF composites are modified on Ni foams as working electrode, and 3 M KOH aqueous solution is used as supporting electrolyte. Fig. S3A† shows the CV curves of PPy-MOF-*x* modified nickel foams measured at a scan rate of 2 mV s<sup>-1</sup>. A pair of redox peaks is observed to appear on the CV curves of the five investigated materials, indicating the characteristics of the pseudocapacitive behavior of the electrode materials caused by the surface faradaic redox reactions, which correspond to the reversible intercalation and deintercalation of OH<sup>-</sup> ions.<sup>39</sup> The process might be represented by the following equation: [Ni<sub>3</sub>(OH)<sub>2</sub>(C<sub>8</sub>H<sub>4</sub>O<sub>4</sub>)<sub>2</sub>(H<sub>2</sub>O)<sub>4</sub>]·2H<sub>2</sub>O + OH<sup>-</sup> - e<sup>-</sup> ↔ [Ni<sub>3</sub>O(OH)(C<sub>8</sub>H<sub>4</sub>O<sub>4</sub>)<sub>2</sub>(H<sub>2</sub>O)<sub>4</sub>]·2H<sub>2</sub>O + H<sub>2</sub>O.<sup>29,36</sup> The curve area of PPy-MOF-*x* also changes with varying the mass of Ni-MOF, in which PPy-MOF-0.2 shows the largest area, indicating the largest specific capacity of PPy-MOF-0.2 in the five composites. GCD curves of PPy-MOF-*x* composites in 3 M KOH aqueous solution at the current density of 0.3 A g<sup>-1</sup> are shown in Fig. S3B.† It can be seen that PPy-MOF-0.2 composite shows longer discharge time, indicating the better capacitive performance, which is consistent with CV results. According to eqn (1), PPy-MOF-0.2 composite possesses the largest specific capacitance at the current density of 0.3 A g<sup>-1</sup> among the various PPy-MOF-*x* composites. Fig. S3C† shows the specific capacitance of the five materials at different current densities. The results indicate that the specific capacitances of different current densities for PPy-MOF-0.2 are much higher than PPy-MOF-0.05, PPy-MOF-0.1, PPy-MOF-0.15, and PPy-MOF-0.3 electrodes under the same conditions, which is in good agreement with CV and GCD results. EIS is a critical technique to study the internal resistance of the electrode and the resistance between the electrode and electrolyte. The equivalent series resistance (ESR) is obtained from the first intersection with the real axis.<sup>40,41</sup> EIS measurements (Fig. S3D†) indicate that PPy-MOF-0.2 composite has a lower ESR, indicating a higher conductivity. Electrochemical results in three-electrode system show that PPy-MOF-0.2 possesses the best capacitive performance among the investigated five PPy-MOF-*x* composites. The electrochemical performances of PPy-MOF-0.2 composite is further compared with Ni-MOF and PPy.

Fig. 4A is the CV curves of PPy, Ni-MOF and PPy-MOF-0.2 composite at the same scan rate of 2 mV s<sup>-1</sup>. As is known, the specific capacitance of the material can be correlated to the average area of the CV curve. Thus, PPy-MOF-0.2 shows the best capacitive behavior among the investigated three materials. Besides that, as shown in Fig. 4B, PPy-MOF-0.2 shows longer duration time than Ni-MOF and PPy in charge-discharge test at the same current density of 0.3 A g<sup>-1</sup>, of which the specific capacitance of PPy-MOF-0.2 is calculated to be 715.6 F g<sup>-1</sup>. According to eqn (1), the specific capacitances of the three materials at different current densities are calculated based on GCD curves, as plotted in Fig. 4C. It can be seen that with the increase of current density, the specific capacitance slowly decreases. Furthermore, the specific capacitance of PPy-MOF-0.2 composite at different current densities is always larger

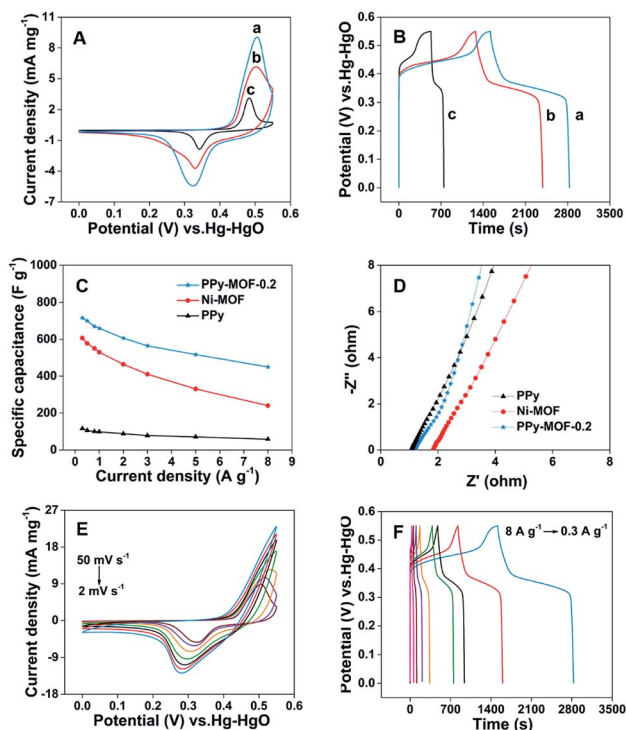


Fig. 4 (A) CV curves of PPy-MOF-0.2 (a), Ni-MOF (b) and PPy (c) modified nickel foams at the scan rate of 2 mV s<sup>-1</sup>. (B) GCD curves of PPy-MOF-0.2 (a), Ni-MOF (b) and PPy (c) modified nickel foams at the current density of 0.3 A g<sup>-1</sup>. (C) Specific capacitances obtained at different current densities. (D) Nyquist plots of PPy-MOF-0.2, Ni-MOF, and PPy modified nickel foams. (E) CV curves of PPy-MOF-0.2 at different scan rates from 2 to 50 mV s<sup>-1</sup>. (F) GCD curves of PPy-MOF-0.2 at different current densities from 0.3 to 8 A g<sup>-1</sup>.

than that for Ni-MOF and PPy, showing the well-performed capacitive behavior. In addition, the specific capacitance of PPy-MOF-0.2 is calculated to be 449.5 F g<sup>-1</sup> at the current density of 8 A g<sup>-1</sup>, retaining 62.8% of the specific capacitance obtained at 0.3 A g<sup>-1</sup>, indicating the good rate capability of PPy-MOF-0.2 composite. Fig. 4D shows the EIS Nyquist plots of PPy-MOF-0.2, Ni-MOF and PPy. It can be clearly seen that PPy displays the lowest ESR among the three investigated materials. Besides that, the ESR of PPy-MOF-0.2 shows lower ESR than Ni-MOF, not only proving the triumph combination of PPy and Ni-MOF, but also confirming that PPy can increase the charge transfer between the electrolyte and active material.<sup>24</sup>

Electrochemical results show that PPy-MOF-0.2 exhibits better capacitive performance than Ni-MOF and PPy. Therefore, more detailed investigation on PPy-MOF-0.2 is performed. Fig. 4E displays the CV curves of PPy-MOF-0.2 at different scan rates ranging from 2 to 50 mV s<sup>-1</sup>. With the increase of scan rate, the area and current density of the CV curves also gradually increase, and a pair of redox peaks appears on all curves, indicating the behavior of pseudocapacitors.<sup>29</sup> Furthermore, the positions of oxidation and reduction peaks shift slightly with increasing the scan rate, which are mainly related to the increment of the internal diffusion resistance and polarization of the electrodes.<sup>42</sup> Fig. 4F shows the GCD curves of PPy-MOF-



0.2 composite at different current densities. It can be seen that a platform appears between 0.3 V and 0.5 V on all curves, showing the existence of redox reaction, further indicating the significant contribution of pseudocapacitance.

To evaluate the practical applications of PPy-MOF, a PPy-MOF//AC ASC is fabricated by utilizing PPy-MOF-0.2 composite, AC and 3 M KOH as the positive electrode, negative electrode and electrolyte, respectively. Fig. 5A shows the CV curves of the assembled ASC at different scan rates from 2 to 50  $\text{mV s}^{-1}$ . A large potential window from 0–1.5 V can be obtained on the fabricated ASC, which is significantly enlarged comparing with the above-mentioned three-electrode system. Besides that, when PPy-MOF-0.2 and AC are employed as positive and negative electrodes to assemble the ASC, the shape of CV curves (Fig. 5A) shows the characteristics of the double layer and faradaic redox behaviors, and no obvious change is observed on the curves with increasing the scan rate from 2 to 50  $\text{mV s}^{-1}$ , indicating a good electrochemical reversibility of the assembled ASC.<sup>42</sup> The ASC is also investigated by GCD test at different current densities from 0.2 to 8  $\text{A g}^{-1}$  (Fig. 5B). Similar to CV results, the assembled ASC can also achieve a high potential of 1.5 V in the GCD test, showing the possible application in practical supercapacitor device. In addition, no obvious platform is observed on the GCD curves, and the non-linearity of the curve also indicates the contribution of the

combination of electrochemical double-layer capacitance and faradaic redox capacitance. The specific capacitance of the ASC can be calculated according to the mass of the active material and the discharge time (Fig. 5C), which is 398.2  $\text{F g}^{-1}$  at the current density of 0.2  $\text{A g}^{-1}$ . The electric conductivity of the ASC is tested by EIS, as shown in Nyquist plot (Fig. 5D). In the high frequency region, the ESR of the electrode material is small, indicating a low contact resistance. In the low frequency region, almost vertical line represents the ion diffusion ability of the PPy-MOF electrode, showing an ideal capacitive behavior.<sup>43,44</sup> The low ESR of the electrode materials and fast ion diffusion at the interface between the electrode and electrolyte are beneficial to the rate performance of the ASC.<sup>44</sup> Additionally, the assembled ASC exhibits an excellent electrochemical cycling stability with 80% capacitance reservation over 10 000 cycles (Fig. 5E). Ragone plot reflects the relationship between energy density and power density of the electrode material. Fig. 5F shows the Ragone plot of the assembled ASC. It can be seen that the assembled ASC delivers an energy density of 120.7  $\text{W h kg}^{-1}$  at a power density of 225.0  $\text{W kg}^{-1}$ , while the energy density reaches 40.1  $\text{W h kg}^{-1}$  when the power density is 1500.6  $\text{W kg}^{-1}$ , which is much higher than recently reported ASCs, such as  $\text{Ni}_x\text{Co}_{1-x}(\text{OH})_2/\text{AC}$  (21.9  $\text{W h kg}^{-1}$  at 348.9  $\text{W kg}^{-1}$ ),<sup>45</sup> Ni-MOF//AC (57.29  $\text{W h kg}^{-1}$  at 160  $\text{W kg}^{-1}$ ),<sup>46</sup> and Ni-MOF/CNTs-5//rGO/ $\text{C}_3\text{N}_4$ -3 (36.6  $\text{W h kg}^{-1}$ , 480  $\text{W kg}^{-1}$ ),<sup>47</sup> and Ni-MOF/PANI//AC (45.6  $\text{W h kg}^{-1}$  at 850.0  $\text{W kg}^{-1}$ ).<sup>42</sup> The superior performance of the PPy-MOF composite may be attributed to the following aspects. First, the addition of PPy facilitates the electron transfer of Ni-MOF structure. Second, the synergistic effect between the Ni-MOF and PPy also contribute to the enhancement in the electrocapacitive performance.

## Conclusions

In summary, PPy-MOF composite composed of Ni-MOF and PPy has been successfully prepared by a facile method and exploited as electrode material for supercapacitor applications, in which PPy can provide quick electron transfer to Ni-MOF. Comparing with Ni-MOF and PPy, the PPy-MOF modified nickel foam shows superior electrochemical performance with a specific capacitance of 715.6  $\text{F g}^{-1}$  at the current density of 0.3  $\text{A g}^{-1}$ . Besides that, a PPy-MOF//AC asymmetric supercapacitor is assembled which exhibits excellent capacitive performance. The ASC can deliver a high energy density of 40.1  $\text{W h kg}^{-1}$  at a power density of 1500.6  $\text{W kg}^{-1}$ . Furthermore, the assembled ASC exhibits remarkable cycling stability. Electrochemical results demonstrate the great potential of the PPy-MOF composite as electrode material in energy storage application.

## Conflicts of interest

There are no conflicts to declare.

## Acknowledgements

This work is supported by the National Natural Science Foundation of China (21501014, 21401012, 21661026), Scientific and

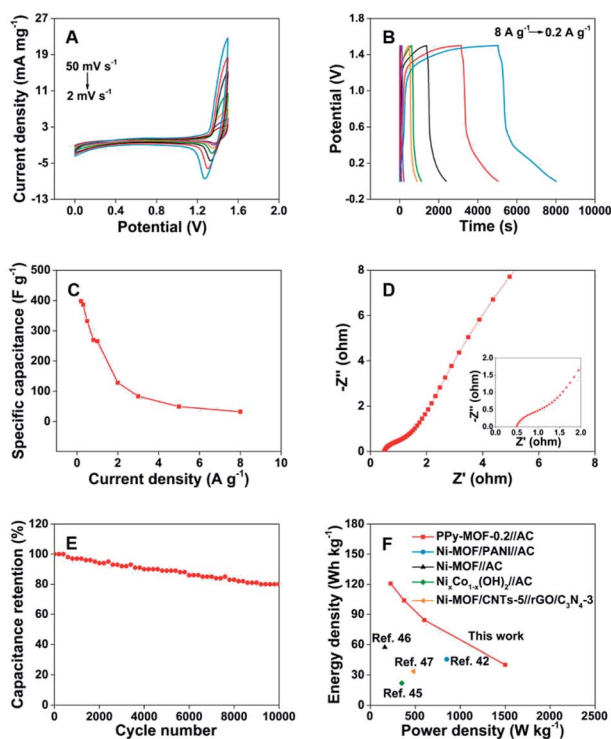


Fig. 5 (A) CV curves of the PPy-MOF//AC ASC at different scan rates from 2 to 50  $\text{mV s}^{-1}$ . (B) GCD curves of the PPy-MOF//AC ASC at different current densities from 0.2 to 8  $\text{A g}^{-1}$ . (C) Specific capacitances obtained from different charge–discharge current densities. (D) Nyquist plot of the assembled ASC. (E) Cycling stability of the ASC at 10  $\text{A g}^{-1}$ . (F) Ragone plots of the assembled ASC comparing with the data previously reported.



Technological Development Program of Jilin Province (20180520157JH), and Education Department of Jilin Province "13th Five-Year" Science Technology Research Project (JJKH20190557KJ).

## References

- 1 Y. Xiao, W. Wei, M. J. Zhang, S. Jiao, Y. C. Shi and S. J. Ding, *ACS Appl. Energy Mater.*, 2019, **2**, 2169–2177.
- 2 A. Balducci, D. Belanger, T. Brousse, J. W. Long and W. Sugimoto, *J. Electrochem. Soc.*, 2017, **164**, A1487–A1488.
- 3 M. Y. Gao, X. F. Wu, H. F. Qiu, Q. F. Zhang, K. K. Huang, S. H. Feng, Y. Yang, T. T. Wang, B. Zhao and Z. L. Liu, *RSC Adv.*, 2018, **8**, 20661–20668.
- 4 K. Asazawa, K. Yamada, H. Tanaka, A. Oka, M. Taniguchi and T. Kobayashi, *Angew. Chem., Int. Ed.*, 2007, **46**, 8024–8027.
- 5 P. Wang, M. Q. Shen, H. Zhou, C. F. Meng and A. H. Yuan, *Small*, 2019, **15**, 1903522.
- 6 Y. D. Zhang, H. Li, J. X. Liu, J. C. Zhang, F. Y. Cheng and J. Chen, *J. Mater. Chem. A*, 2019, **7**, 20958–20964.
- 7 X. C. Xie, K. J. Huang and X. Wu, *J. Mater. Chem. A*, 2018, **6**, 6754–6771.
- 8 J. Y. Cheng, S. M. Chen, D. Chen, L. B. Dong, J. J. Wang, T. L. Zhang, T. P. Jiao, B. Liu, H. Wang, J. J. Kai, D. Q. Zhang, G. P. Zheng, L. J. Zhi, F. Y. Kang and W. J. Zhang, *J. Mater. Chem. A*, 2018, **6**, 20254–20266.
- 9 S. Y. Wu, X. F. Wu, G. D. Wang, L. X. Li, K. K. Tang, K. K. Huang, S. H. Feng, X. T. Dong, Z. L. Liu and B. Zhao, *Electrochim. Acta*, 2016, **218**, 66–73.
- 10 G. L. Zhu, H. Wen, M. Ma, W. Y. Wang, L. Yang, L. C. Wang, X. F. Shi, X. W. Cheng, X. P. Sun and Y. D. Yao, *Chem. Commun.*, 2018, **54**, 10499–10502.
- 11 T. Pham, K. A. Forrest, R. Banerjee, G. Orcajo, J. Eckert and B. Space, *J. Phys. Chem. C*, 2014, **119**, 1078–1090.
- 12 W. B. Lu and X. F. Wu, *New J. Chem.*, 2018, **42**, 3180–3183.
- 13 P. García-García, M. Müller and A. Corma, *Chem. Sci.*, 2014, **5**, 2979–3007.
- 14 E. Coronado and G. M. Espallargas, *Chem. Soc. Rev.*, 2013, **42**, 1525–1539.
- 15 A. V. Vinogradov, H. Zaake-Hertling, E. Hey-Hawkins, A. V. Agafonov, G. A. Seisenbaeva, V. G. Kessler and V. V. Vinogradov, *Chem. Commun.*, 2014, **50**, 10210–10213.
- 16 K. Liu, L. M. Deng, H. D. Li, Y. X. Bao, Z. Y. Xiao, B. Li, Q. Zhou, Y. L. Geng and L. Wang, *J. Solid State Chem.*, 2019, **275**, 1–7.
- 17 A. Morozan and F. Jaouen, *Energy Environ. Sci.*, 2012, **5**, 9269–9290.
- 18 Y. J. Zhou, Z. M. Mao, W. Wang, Z. K. Yang and X. Liu, *ACS Appl. Mater. Interfaces*, 2016, **8**, 28904–28916.
- 19 S. Peng, L. L. Fan, C. Z. Wei, X. H. Liu, H. W. Zhang, W. L. Xu and J. Xu, *Carbohydr. Polym.*, 2017, **157**, 344–352.
- 20 Q. Lu, J. Liu, X. Y. Wang, B. Lu, M. F. Chen and M. H. Liu, *J. Energy Storage*, 2018, **18**, 62–71.
- 21 Y. Y. Tian, X. F. Song, J. Liu, L. P. Zhao, P. Zhang and L. Gao, *Adv. Mater. Interfaces*, 2019, **6**, 1900162.
- 22 S. Grover, S. Shekhar, R. K. Sharma and G. Singh, *Electrochim. Acta*, 2014, **116**, 137–145.
- 23 A. Bahloul, B. Nessark, E. Briot, H. Groult, A. Mauger, K. Zaghbi and C. M. Julien, *J. Power Sources*, 2013, **240**, 267–272.
- 24 Y. Z. Liu, N. Xu, W. C. Chen, X. L. Wang, C. Y. Sun and Z. M. Su, *Dalton Trans.*, 2018, **47**, 13472–13478.
- 25 R. Z. Hou, M. Miao, Q. Y. Wang, T. Yue, H. F. Liu, H. S. Park, K. Qi and B. Y. Xia, *Adv. Energy Mater.*, 2019, **10**, 1901892.
- 26 K. Qi, R. Z. Hou, S. Zaman, Y. B. Qiu, B. Y. Xia and H. W. Duan, *ACS Appl. Mater. Interfaces*, 2018, **10**, 18021–18028.
- 27 X. T. Xu, J. Tang, H. Y. Qian, S. J. Hou, Y. Bando, M. S. A. Hossain, L. K. Pan and Y. Yamauchi, *ACS Appl. Mater. Interfaces*, 2017, **9**, 38737–38744.
- 28 H. N. Wang, M. Zhang, A. M. Zhang, F. C. Shen, X. K. Wang, S. N. Sun, Y. J. Chen and Y. Q. Lan, *ACS Appl. Mater. Interfaces*, 2018, **10**, 32265–32270.
- 29 Y. Yan, P. Gu, S. S. Zheng, M. B. Zheng, H. Pang and H. G. Xue, *J. Mater. Chem. A*, 2016, **4**, 19078–19085.
- 30 H. Khan, K. Malook and M. Shah, *J. Mater. Sci.: Mater. Electron.*, 2018, **29**, 9090–9098.
- 31 S. W. Gao, Y. W. Sui, F. X. Wei, J. Q. Qi, Q. K. Meng and Y. Z. He, *J. Mater. Sci.*, 2018, **53**, 6807–6818.
- 32 S. J. Hou, X. T. Xu, M. Wang, Y. Q. Xu, T. Lu, Y. F. Yao and L. K. Pan, *J. Mater. Chem. A*, 2017, **5**, 19054–19061.
- 33 C. Chen, M. K. Wu, K. Tao, J. J. Zhou, Y. L. Li, X. Han and L. Han, *Dalton Trans.*, 2018, **47**, 5639–5645.
- 34 M. A. A. M. Abdah, N. M. M. A. Edris, S. Kulandaivalu, N. A. Rahman and Y. Sulaiman, *Int. J. Hydrogen Energy*, 2018, **43**, 17328–17337.
- 35 J. W. Lee, T. Ahn, D. Soundararajan, J. M. Ko and J. D. Kim, *Chem. Commun.*, 2011, **47**, 6305–6307.
- 36 J. Yang, P. X. Xiong, C. Zheng, H. Y. Qiu and M. D. Wei, *J. Mater. Chem. A*, 2014, **2**, 16640–16644.
- 37 J. Wang, Q. Zhong, Y. H. Xiong, D. Y. Cheng, Y. Q. Zeng and Y. F. Bu, *Appl. Surf. Sci.*, 2019, **483**, 1158–1165.
- 38 Y. Z. Wang, Y. X. Liu, H. Q. Wang, W. Liu, Y. Li, J. F. Zhang, H. Hou and J. L. Yang, *ACS Appl. Energy Mater.*, 2019, **2**, 2063–2071.
- 39 C. Y. Yang, X. Y. Li, L. Yu, X. J. Liu, J. Yang and M. D. Wei, *Chem. Commun.*, 2020, **56**, 1803–1806.
- 40 C. Y. Yang, P. F. Zhang, A. Nautiyal, S. H. Li, N. Liu, J. L. Yin, K. L. Deng and X. Y. Zhang, *ACS Appl. Mater. Interfaces*, 2019, **11**, 4258–4267.
- 41 Y. Jiao, G. Chen, D. H. Chen, J. Pei and Y. Y. Hu, *J. Mater. Chem. A*, 2017, **5**, 23744–23752.
- 42 Q. H. Cheng, K. Tao, X. Han, Y. J. Yang, Z. Yang, Q. X. Ma and L. Han, *Dalton Trans.*, 2019, **48**, 4119–4123.
- 43 F. Jiang, Z. S. Ge, B. Niu, M. Y. Yuan, S. Y. Wei and M. Li, *J. Appl. Polym. Sci.*, 2019, **136**, 47816.
- 44 C. Sarkar, J. Nath, S. Bhuyan and S. K. Dolui, *ChemistrySelect*, 2019, **4**, 2529–2537.
- 45 S. H. He, Z. P. Li, J. Q. Wang, P. Wen, J. C. Gao, L. M. Ma, Z. G. Yang and S. R. Yang, *RSC Adv.*, 2016, **6**, 49478–49486.
- 46 C. R. Zhang, Q. Zhang, K. Zhang, Z. Y. Xiao, Y. Yang and L. Wang, *RSC Adv.*, 2018, **8**, 17747–17753.
- 47 P. Wen, P. W. Gong, J. F. Sun, J. Q. Wang and S. R. Yang, *J. Mater. Chem. A*, 2015, **3**, 13874–13883.

